Simple shear behavior and constitutive modeling of 304 stainless steel over a wide range of strain rates and temperatures

B. Jia [a,b,*], A. Rusinek [b,c], R. Pesci [b], R. Bernier [b], S. Bahi [b], A. Bendarma [d], P. Wood [e]

[a] ENSAM-Arts et Métiers ParisTech, Laboratory of Design, Manufacturing and Control (LCFC), 57070 Metz, France
[b] Lorraine University, ENSAM-Arts et Métiers ParisTech, Laboratory of Microstructure Studies and Mechanics of Materials (LEM3), UMR CNRS 7239, 57078 Metz, France
[c] Chair of Excellence, Department of Mechanical Engineering, University Carlos III of Madrid, Avda. Universidad 30, 28911 Leganés, Madrid, Spain
[d] International University of Agadir, Universiapolis, Ecole Polytechnique d'Agadir Bab Al Madina, Agadir, Morocco
[e] Institute for Innovation in Sustainable Engineering, College of Engineering and Technology, University of Derby, Quaker Way, Derby, DE1 3HD, UK

A B S T R A C T

A novel single shear specimen (SSS) together with a correction coefficient method is used to study the deformation behavior of a 304 stainless steel under shear loadings. Shear stress-shear strain relations over a wide range of shear strain rates (0.001 to 39000 s^{-1}) at three initial temperatures (77 to 473 K) are obtained experimentally. The effects of strain rate and temperature on the flow stress curves are determined. With increasing strain rate or temperature, the strain hardening rate decreases continuously. At the maximum strain rate of 39000 s^{-1}, negative strain hardening rates are observed. At very high strain rates above 13000 s^{-1}, a sharp increase in flow stress is observed, indicating a rapid rise in strain rate sensitivity. The fracture morphology of post-mortem specimens is analyzed and no well-developed adiabatic shear bands are observed. This may be due to the shear-tension stress state without hydrostatic pressure in the fracture process. Based on the experimentally obtained shear stress-shear strain curves, parameters of a modified Johnson-Cook (MJC) model are determined. A good agreement between experiments and model predictions is found, with an average error of 3.9%. Using finite element analysis, distributions of stress and strain components in the specimen shear zone is analyzed. It is found that the shear stress and shear strain play dominant roles, and a simple shear stress state with low stress triaxiality (0.015) and Lode angle parameter (0.014) is obtained.

1. Introduction

In the class of Transformation Induced Plasticity (TRIP) steels [1], 304 Austenitic Stainless Steel (ASS) has a unique combination of high strength and high ductility [2]. The two traditionally contradictory mechanical properties are achieved through an austenite to martensite phase transformation $\gamma_{fcc} \rightarrow \alpha_{bcc}$, leading to an increase in both strain hardening rate and ductility. These properties make 304 ASS extensively used in transport, civil, defense and other industrial fields. In service, the material may be subjected to various loading regimes, such as vehicle crashworthiness, sheet metal forming and high speed machining, with local strain rates reaching 10^5 s^{-1}. Therefore, an accurate experimental characterization of the material's behavior over a wide range of temperatures and strain rates is highly desired.

In recent years, much work has been done to study the deformation behavior of 304 ASS under different temperatures. Byun et al. [3] investigated the tensile behavior of 304 ASS over temperatures between 123 and 723 K. At elevated temperatures, the deformation process is dominated by dislocation slip. With increasing strain, the strain hardening rate decreases monotonically. At room temperature or below, however, the deformation mechanism is a competition between martensitic transformation and dislocation slip, and the flow stress curves exhibit an S-shape and a two-stage hardening phenomenon. The characteristic second stage hardening behavior was also observed by other researchers in different TRIP steels [4–7]. Zheng and Yu [5] studied the tensile behavior of 304 ASS at temperatures between 20 and 293 K. The yield stress at the lowest temperature of 20 K was found to be significantly higher than for the other temperatures. This is attributed to the thermally induced martensitic transformation before tests [5]. The effect of strain rate on the deformation behavior of 304 ASS is also

different from the commonly used metallic materials deformed by dislocation slip. According to the work of Lichtenfeld et al. [8], strain rate sensitivity of 304 ASS may vary with plastic strains. At the initial stage of deformation ($\varepsilon_p = 0.05$), no phase transformation occurs and the deformation process is controlled by dislocation slip. Hence, the tensile stress increases with increasing strain rate as the time available for a dislocation to wait in front of an obstacle for the additional thermal energy is reduced. At large strains ($\varepsilon_p = 0.35$), a negative strain rate sensitivity is observed in the quasi-static strain rate regime (10^{-4} to 10^{-1} s^{-1}) and then becomes positive in the dynamic strain rate regime (1 to 400 s^{-1}). This is because with increasing strain rate, martensitic transformation is gradually reduced by adiabatic heating, and the corresponding strength decreases [9–11]. A similar fact was observed by Jia et al. during uniaxial compression tests at strain rates between 10^{-3} and 3270 s^{-1} [12].

From the literature review, considerable research has been devoted to investigating the deformation behavior of 304 ASS under different conditions, and mainly focus on uniaxial tension or compression stress states. Although dynamic shear loading is frequently encountered, such as sheet metal forming, high speed machining, ballistic penetration and perforation, only a few studies can be found in the open literature. According to a comparison of flow stress curves obtained from simple shear and uniaxial compression tests, Xu et al. [13,14] showed that the stress state does have an important effect on material behavior. Although stress-strain relations derived from uniaxial tension or compression tests are often used to simulate shear deformation process, the accuracy of such a method may be questionable [14]. For an accurate computation of shear dominated engineering applications, the constitutive model derived from shear tests should be used.

Another limitation of the existing research on characterizing deformation behavior of 304 ASS is the testing strain rate regime. Generally, the studies mentioned above are limited to within 4000 s^{-1} using the high-speed testing machine or the Split Hopkinson Bar apparatus, and do not work well if the strain rate is very high above 10^4 s^{-1}. Follansbee and Kocks [15] studied the deformation behavior of oxygen-free high conductivity (OFHC) copper and a rapid increase in flow stress was observed when the strain rate approached 10^4 s^{-1}. Similar phenomena were also reported by Tong et al. [16] and Huang and Clifton [17], as shown in Fig. 1. Correspondingly, the strain rate sensitivity (defined as $m_s = \frac{\partial(\log\sigma)}{\partial(\log\dot{\varepsilon})}$, where σ is the flow stress and $\dot{\varepsilon}$ denotes the plastic strain rate) under very high strain rates above 10^4 s^{-1} is different from that at low strain rates. Some researchers [18–20] thought this was due to the transition of rate-controlling mechanism from the thermally activated dislocation motion at low strain rates to the viscous drag effect at very high strain rates, while some others [21–23] attributed this phenomenon to the enhanced dislocation accumulation rate at very high strain rates. Therefore, the investigations mentioned in the previous paragraphs may not be capable of capturing the real deformation behavior of 304 ASS over a wide range of strain rates, especially at the very high loading conditions. Experimental characterization of the material's behavior over a wide range of strain rates and temperatures is necessary.

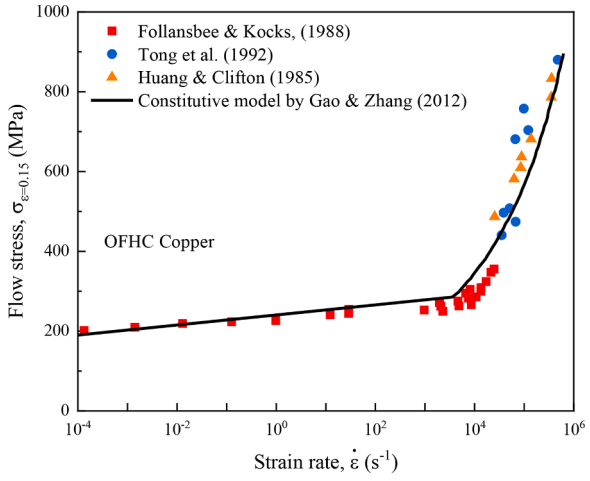

Fig. 1. Variation of flow stress with strain rates in OFHC copper at room temperature [15–17,24].

Recently, a new S-shaped shear specimen was developed by Arab et al. [25]. Compared to the traditional hat shape specimen, a homogeneous distribution of stress components is achieved in the specimen shear zone, and the measured flow stress curves represent deformation behavior of the tested material accurately. Later, a similar geometry called single shear specimen (SSS) was proposed by Jia et al. [26] to study the deformation behavior of bulk metals under simple shear stress state. Shear stress-shear strain relations can be determined precisely using a correction coefficient method. Together with a classical SHPB device, the SSS specimen can be tested conveniently at high (10^3 $s^{-1} \leq \dot{\gamma} \leq 10^4$ s^{-1}) and very high (10^4 $s^{-1} \leq \dot{\gamma} \leq 10^5$ s^{-1}) strain rates. In the present work, the deformation behavior of a 304 ASS was investigated systematically over a wide range of strain rates (10^{-3} to 39000 s^{-1}) at three different temperatures (77 K, 293 K and 473 K). In section 2, SSS specimen and the corresponding testing technique is introduced. Experimental results in terms of shear stress-shear strain relations and fracture morphology characteristics are presented and discussed in section 3. In section 4, a modified Johnson-Cook (MJC) model considering the strain rate and temperature-dependent strain hardening behavior and the viscous drag effect is established. The capability of the MJC model is evaluated through numerical simulations of dynamic shear tests. Stress state in the specimen shear zone is analyzed. Finally, the main findings are summarized in Section 5.

2. Experimental technique

2.1. Material and SSS specimen

In this work, the newly-designed SSS specimen is tested over a wide range of strain rates at different temperatures to study the deformation behavior of 304 ASS. A detailed description of the SSS specimen and the corresponding testing technique may be found in the work of Jia et al. [26]. For completeness, the specimen geometry, the quasi-static and dynamic loading principles are briefly introduced again.

A schematic diagram of the SSS specimen is shown in Fig. 2. It is a cylinder with two "*L*"-shaped slots machined centrosymmetrically. The shear zone with a height (*H*) of 1.5 mm and a width (*L*) of 0.5 mm is located between the two slots. The shear zone width may vary between 0.3 and 1.0 mm to obtain a wider range of strain rates. Between the shear zone and the support structure, fillets with a radius of 0.1 mm are machined to reduce stress concentration. The specimen is designed as a single part without clamp grips, fixtures or screws. Thus, it can be loaded conveniently with the universal testing machine for quasi-static tests and the classical SHPB apparatus for dynamic tests.

The material considered herein is a commercial stainless steel rod (dimensions: $\Phi 10 \times 1000$ mm^3). According to the manufacturer's specification, the chemical composition is given in Table 1. All SSS specimens were machined along the axial direction of the rod by wire electrical discharge machining (WEDM) to avoid martensitic transformation.

2.2. Quasi-static shear tests

Quasi-static shear tests were conducted using a Zwick/Roell 100kN universal testing machine with an environmental chamber. Two strain rates (10^{-3} s^{-1} and 10^{-1} s^{-1}) and three temperatures (77K, 293K, and 473K) were considered. By applying a force $F(t)$ with a constant velocity $V(t)$ on the top surface of the specimen, the nominal shear strain rate $\dot{\gamma}_{nominal}(t)$, nominal shear strain $\gamma_{nominal}(t)$ and nominal shear stress

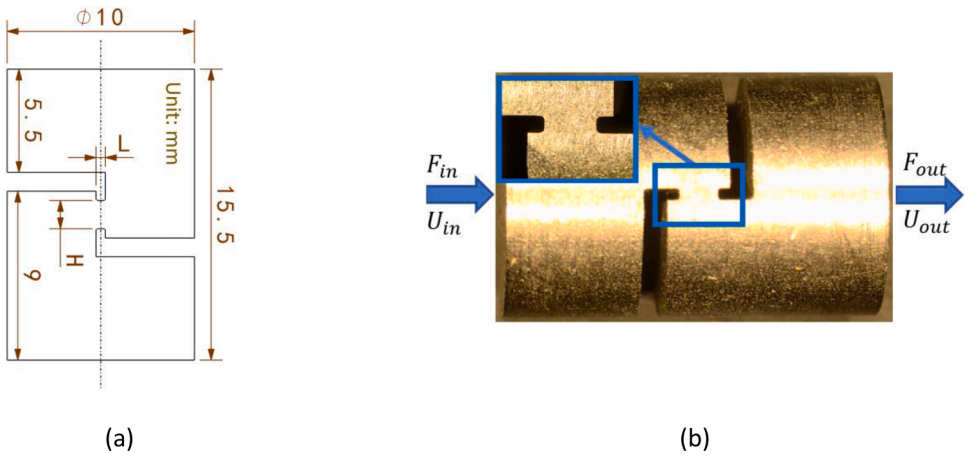

Fig. 2. (a) Schematic diagram and (b) practical arrangement of the SSS specimen.

Table 1
Chemical composition of the studied 304 ASS (wt, %).

Material	C	Cr	Mn	N	Ni	Co	Cu	Fe
304 ASS	0.018	17.60	1.64	0.72	8.04	0.20	0.33	Bal

$\tau_{nominal}(t)$ in the specimen shear zone can be calculated by

$$\begin{cases} \dot{\gamma}_{nominal}(t) = \dfrac{V(t)}{L} \\ \gamma_{nominal}(t) = \displaystyle\int \dot{\gamma}_{nominal}(t)dt \\ \tau_{nominal}(t) = \dfrac{F(t)}{A_{sz}} \end{cases} \tag{1}$$

where A_{sz} is the cross-sectional area of the shear zone.

2.3. Dynamic shear tests

Dynamic shear tests at six strain rates (3000 s^{-1}, 6000 s^{-1}, 13000 s^{-1}, 22000 s^{-1}, 26000 s^{-1} and 39000 s^{-1}) and three temperatures (77K, 293K and 473K) were carried out using a classical SHPB apparatus, Fig. 3. The SSS specimen is sandwiched between the incident and the transmitted bars without any clamping devices. To minimize friction between the specimen and the SHPB bars, the specimen end faces were coated with molybdenum disulphide grease. For shear tests at elevated temperatures, a heating furnace coupled to the SHPB device was used. For shear tests at low temperatures, the specimen was immersed in a cooling chamber filled with liquid nitrogen, corresponding to a temperature of 77 K. During shear tests at high or low temperatures, the temperature distribution within the specimen is uniform with a maximum fluctuation of 1.2 K. A detailed description of the SHPB apparatus may be found in the work of Zhong et al. [27].

According to the one-dimensional wave propagation theory, the forces $F_1(t)$ and $F_2(t)$ and displacements $U_1(t)$ and $U_2(t)$ at the specimen/bar interfaces can be calculated by

$$\begin{cases} F_1(t) = EA(\varepsilon_I(t) + \varepsilon_R(t)) \\ F_2(t) = EA\varepsilon_T(t) \end{cases} \tag{2}$$

$$\begin{cases} U_1(t) = C\displaystyle\int_0^t (\varepsilon_I(t) - \varepsilon_R(t))dt \\ U_2(t) = C\displaystyle\int_0^t \varepsilon_T(t)dt \end{cases} \tag{3}$$

where E, A and C are the Young's modulus, the cross-sectional area and the elastic wave propagation speed of the SHPB bars, respectively. $\varepsilon_I(t)$, $\varepsilon_R(t)$ and $\varepsilon_T(t)$ are respectively the incident, reflected and transmitted strain wave signals. The nominal shear strain rate $\dot{\gamma}_{nominal}(t)$, nominal shear strain $\gamma_{nominal}(t)$ and nominal shear stress $\tau_{nominal}(t)$ are calculated by the following equations.

$$\begin{cases} \gamma_{nominal}(t) = \dfrac{\Delta U}{L} = \dfrac{U_1(t) - U_2(t)}{L} \\ \dot{\gamma}_{nominal}(t) = \dfrac{d\gamma_{nominal}(t)}{dt} \\ \tau_{nominal}(t) = \dfrac{F_{average}}{A_{sz}} = \dfrac{F_1 + F_2}{2A_{sz}} \end{cases} \tag{4}$$

According to the work of Rusinek and Klepaczko [28], the determined $\tau_{nominal} - \gamma_{nominal}$ relations by Eqs. (1-4) represent the overall response of the whole specimen instead of the real shear behavior of the tested material. This is due to the non-uniform distribution of stress components in the specimen shear zone [28] and the stiffness

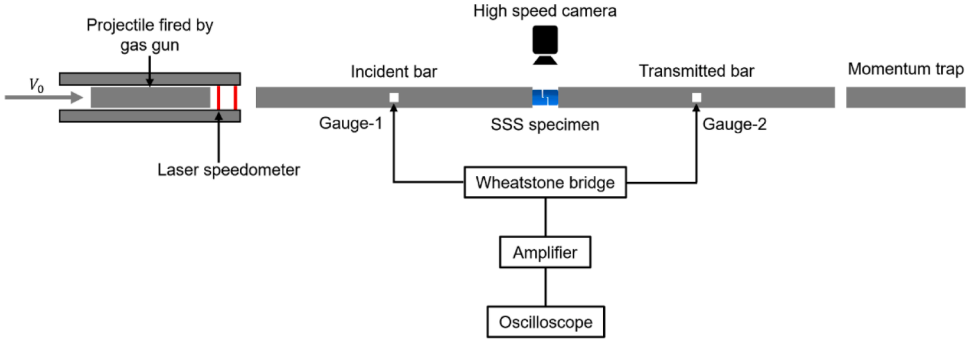

Fig. 3. Schematic presentation of the classical SHPB apparatus.

exaggeration of areas outside the shear zone [29,30]. Hence, the correction coefficient method proposed by Campbell and Ferguson [31] is used to extract the real shear behavior from the $\tau_{nominal} - \gamma_{nominal}$ data. The quantities are defined as follow:

$$\begin{cases} \gamma(t) = \overline{\lambda_\gamma}\left(\gamma_{nominal}(t) - y_{yield}\right) \\ \dot{\gamma}(t) = \overline{\lambda_\gamma}\dot{\gamma}_{nominal}(t) \\ \tau(t) = \overline{\lambda_\tau}\tau_{nominal}(t) \end{cases} \tag{5}$$

where y_{yield} refers to the nominal shear strain at which the specimen starts to yield. $\overline{\lambda_\gamma}$ and $\overline{\lambda_\tau}$ are the average correction coefficients for shear strain and shear stress, respectively.

Values of the two parameters for SSS specimens with different shear zone widths L are shown in Table 2. According to the work of Rusinek and Klepaczko [28], Guo and Li [32] and Fras [33], values of the correction coefficients are only functions of the specimen geometry and do not change significantly for different kinds of tested materials, such as different yield stress levels and strain hardening rates. In the present work, it has been further verified numerically that values of the correction coefficients are strong functions of the specimen geometry but keep the same for different testing conditions.

3. Experimental results and discussion

3.1. Shear stress-shear strain relations

Under quasi-static strain rates, shear stress-shear strain curves at three different temperatures are shown in Fig. 4. The temperature has a significant effect on the strain hardening behavior: at 77 K, the flow stress curves show a positive strain hardening rate; with increasing temperature from 77 to 473 K, the strain hardening rate decreases monotonically; at 473 K, no strain hardening phenomenon is observed and flow stress curves remain constant at different shear strains. The average strain hardening rates for 77, 293 and 473 K are 484, 300 and 67 MPa/unit strain, respectively. Compared to temperature, no obvious effect of strain rate on the strain hardening behavior is observed. The effect of temperature on the flow stress can be clearly seen from the curves. Under both strain rates, the flow stress decreases evidently with increasing temperature. At 77 K and shear strain of 0.2, the flow stress is 776 MPa; the value reduces by 30.5% and 50.3% respectively for 293 and 423 K. Concerning the effect of strain rate on the flow stress, no difference is observed between 0.001 and 0.1 s^{-1}.

Under dynamic loadings, shear tests at strain rates ranging from 3000 to 39000 s^{-1} were carried out. SSS specimens with different shear zone width L were used for various strain rate regimes: $L = 1$ mm for $\dot{\gamma} \leq$ 15000 s^{-1}; $L = 0.5$ mm for 15000 $s^{-1} < \dot{\gamma} <$30000 s^{-1}; $L = 0.3$ mm for 30000 $s^{-1} \leq \dot{\gamma}$. A typical $\tau_{nominal} - \gamma_{nominal}$ curve at nominal shear strain rate of 12000 s^{-1} is shown in Fig. 5 (a). It is observed that the yield stress is close to 500 MPa; after yielding, the flow stress increases continuously with an average strain hardening rate of 265 MPa/unit strain; damage initiates at $\gamma_{nominal} = 0.64$ and then develops quickly; finally, specimen fracture is observed at $\gamma_{nominal} = 1.05$. During the entire plastic deformation process, the nominal shear strain rate remains almost constant at 12000 s^{-1}. According to Eq. (5), the $\tau_{nominal} - \gamma_{nominal}$ curve is converted into the real $\tau - \gamma$ curve, Fig. 5 (b). It is seen that correction of the nominal curve leads to an increase in both the shear stress and the shear strain. Moreover, the shear stress-shear strain relation may be converted into the equivalent stress-equivalent strain ($\sigma - \varepsilon$) curve using a Von-Mises approach.

$$\sigma = \sqrt{3}\tau \tag{6}$$

$$\varepsilon = \gamma \Big/ \sqrt{3} \tag{7}$$

A high speed camera was used to monitor the deformation process with frame rate of 125000 fps. The relative displacement between the top and bottom surfaces of the specimen was calculated using software Tracker (http://physlets.org/tracker/) and then compared to the results obtained from strain gauges on the SHPB bars. It is seen from Fig. 6 that the two curves agree with each other well. Moreover, during the whole plastic deformation process, the specimen moves laterally along the SHPB bars and no rotation is observed. Hence, the single shear zone design without any clamping devices is feasible for dynamic tests. In addition, in the curve measured by the strain gauges, damage initiates at 70.44 μs; while in the curve recorded by the camera, an obvious fracture is observed at 80 μs. Considering the time needed for damage propagation and the time interval between two camera frames (8 μs), the failure processes measured by the strain gauges and by the high speed camera should be consistent. In summary, the experimentally obtained displacement-time data by strain gauges are valid.

Shear stress-shear strain ($\tau - \gamma$) curves obtained under six strain rates (3000 to 39000 s^{-1}) at three temperatures (77 to 473 K) are shown in Fig. 7. It is seen that the effect of temperature on the strain hardening rate and the flow stress is similar to that under quasi-static strain rates: both of them decrease gradually with increasing temperature. At the maximum temperature of 473 K, the flow stress curves either remain constant at different strains or display a negative strain hardening behavior. With increasing strain rate, the flow stress increases abruptly. For example, from 3000 to 39000 s^{-1} and at shear strain of 0.1, the flow stresses increase by 38.4%, 27.9% and 31.7% for 77, 293 and 473 K, respectively. Concerning the effect of strain rate on the strain hardening rate, the values remain positive at strain rates below 26000 s^{-1} but become negative at the maximum strain rate of 39000 s^{-1}.

To study the effect of temperature and strain rate on the flow stress more in details, the variation of flow stress with strain rate at three temperatures is shown in Fig. 8 (a). Both strain rate hardening and thermal softening are observed. Under quasi-static strain rates, the flow stresses remain constant at all the three temperatures; from 0.1 to 6000 s^{-1}, a slight increase in flow stress is identified; at higher strain rates, a rapid increase in flow stress is observed, indicating a sharp rise in strain rate sensitivity. For example, from 13000 to 39000 s^{-1} at 77, 293 and 473 K, the corresponding flow stress increased by 30.5%, 12.7% and 16.0%, respectively. The observed strain rate and temperature sensitivities in 304 ASS can be explained according to the theory of thermally-activated dislocation motion, Fig. 9. The total flow stress can be decomposed into the athermal part σ_μ and the thermal part σ^*. In the former, it remains constant at different strain rates and temperatures. In the latter, the barriers to dislocation motion can be readily overcome with the aid of thermal activation energy. Moreover, with increasing strain rate, the time available for dislocations to accumulate vigorous thermal fluctuation to overcome the barriers reduces. Hence, higher effective stress is needed for dislocation motion to remain active. Therefore, with decreasing temperature or increasing strain rate, the flow stress increases continuously. At very high strain rates, due to the interactions of dislocation-phonon and dislocation-electron, the viscous drag effect surpasses the thermal activation mechanism and becomes dominant. Hence, a dramatic flow stress increase is observed. In addition, Follansbee and Kocks investigated the deformation behavior of pure copper at strain rates between 10^{-4} and 10^4 s^{-1} [15]. An enhanced dislocation accumulation rate is observed at strain rates above 10^3 s^{-1} and it leads to the apparent strong flow stress increase. Therefore, enhanced dislocation accumulation rate instead of viscous drag is another likely explanation for the strong strain rate sensitivity observed at very high strain rates.

Table 2
Correction coefficients for the SSS specimen with different shear zone width L.

Specimen shear zone width L (mm)	$\overline{\lambda_\gamma}$	$\overline{\lambda_\tau}$
0.3	0.860	1.055
0.5	0.870	1.070
1.0	1.050	1.120

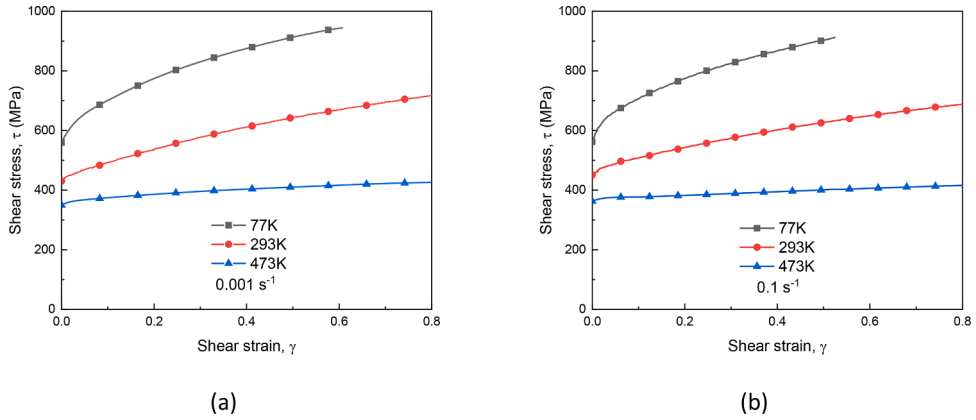

Fig. 4. Shear stress-shear strain curves of 304 ASS at indicated temperatures under quasi-static strain rates: (a) 0.001 s^{-1} and (b) 0.1 s^{-1}.

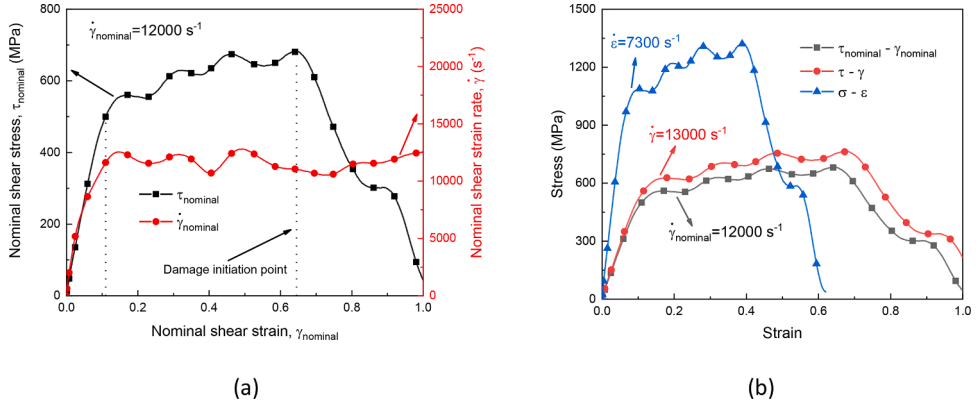

Fig. 5. (a) Nominal shear stress-nominal shear strain curve and (b) correction of the nominal data into the real shear relation and the equivalent stress-equivalent strain curve.

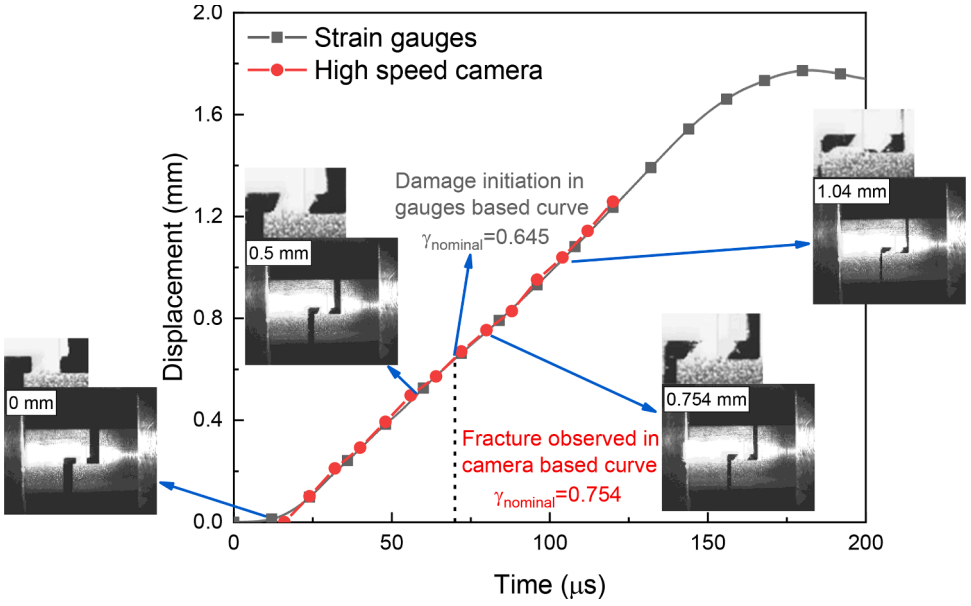

Fig. 6. Comparison of displacement-time curves between by strain gauges on the SHPB bars and by a high speed camera.

To investigate the strain hardening behavior of 304 ASS quantitatively, the plastic deformation stage in the flow stress curves is fitted linearly and the slope is regarded as the average strain hardening rate. The evolution of the average strain hardening rate as a function of strain rate at three temperatures is shown in Fig. 8 (b). It is seen that with increasing temperature, the average strain hardening rate decreases. For example, at 0.001 s^{-1} and 77 K, the average strain hardening rate is 695 MPa; then the value reduces by 42.4% and 88.8% at 293 and 473 K,

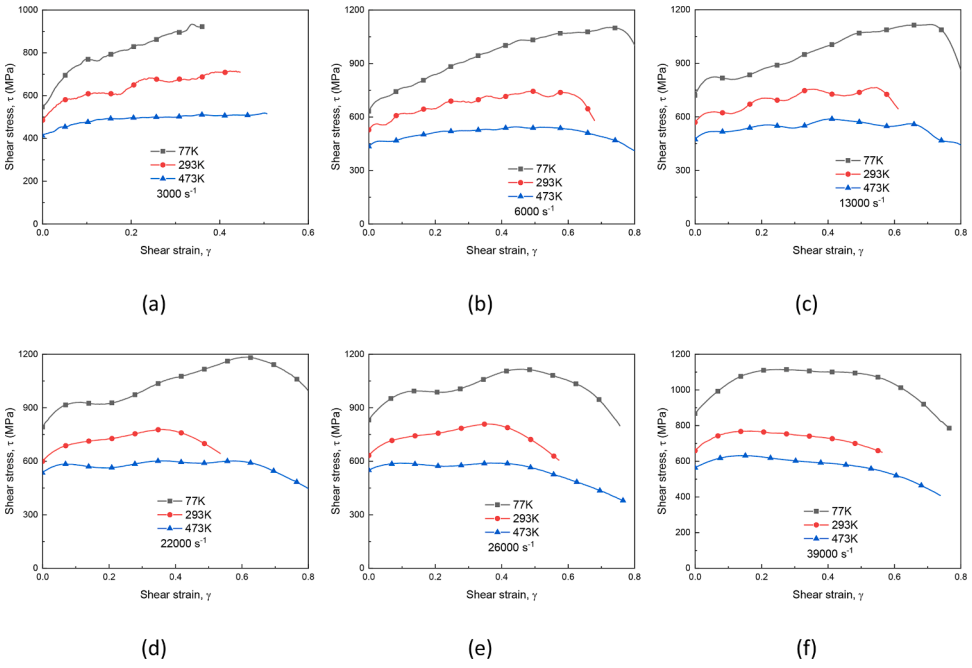

Fig. 7. Shear stress-shear strain curves at indicated temperatures under dynamic strain rates: (a) 3000 s^{-1}, (b) 6000 s^{-1}, (c) 13000 s^{-1}, (d) 22000 s^{-1}, (e) 26000 s^{-1} and (f) 39000 s^{-1}.

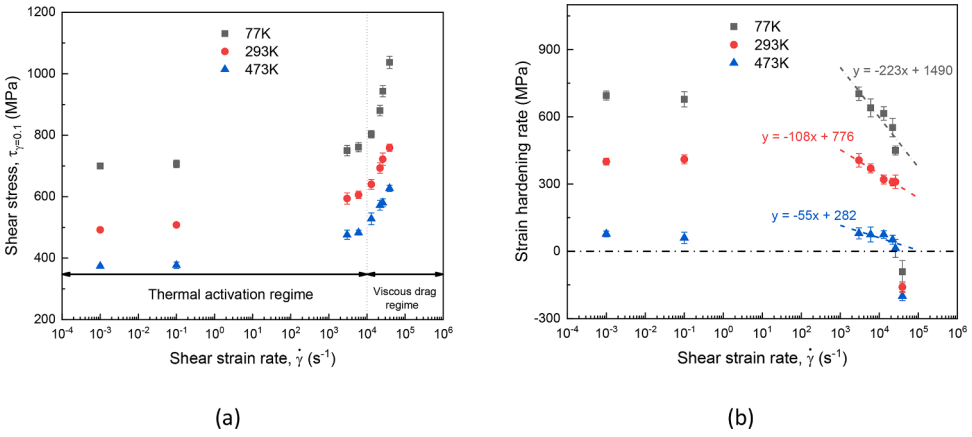

Fig. 8. Variation of (a) flow stress level and (b) strain hardening rate with strain rates at three temperatures.

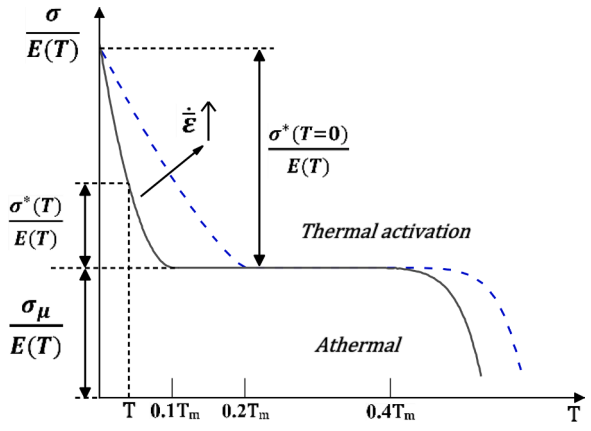

Fig. 9. Decomposition of the total flow stress σ into the thermally activated part σ^* and the athermal part σ_μ [34].

respectively. The effect of strain rate on the average strain hardening rate can be divided into two regimes: from 0.001 to 3000 s^{-1}, it remains almost constant; at higher strain rates above 3000 s^{-1}, it decreases monotonically for all three temperatures. Especially, at the maximum strain rate of 39000 s^{-1}, the strain hardening rates become negative, indicating a decrease of flow stress with increasing strain. It is noteworthy that although the strain hardening rate is elevated at lower temperatures, it declines more qucikly with strain rate than at higher temperatures. For example, from 3000 to 26000 s^{-1}, the evolution of strain hardening rate is fitted linearly and the slopes of the curves are -223, -108 and -55.3 MPa/unit strain rate for 77, 293 and 473 K, respectively. The evolution of strain hardening rate with strain rate or temperature can be explained according to the thermally activated dislocation motion theory too [31,35]. Strain hardening originates from a competition between the generation, multiplication and annihilation of dislocations. At elevated temperature, dislocations can overcome the barriers encountered more easily with the aid of thermal activation energy. Hence, both the thermal part σ^* of the total flow stress and the corresponding strain hardening rate decrease. Under dynamic strain

rates, due to adiabatic heating, the strain hardening rate is weakened [36]. In addition, with increasing temperature, the ratio of the thermal part σ^* to the total flow stress declines. Hence, during dynamic shear tests, the effect of strain rate on the strain hardening rate is less sensitive at elevated temperature.

3.2. Fracture morphology characteristics

To better explain the effect of strain rate on the deformation behavior of 304 ASS, fracture patterns of SSS specimens under both quasi-static and dynamic loadings at room temperature are shown in Fig. 10.

The typical fracture morphology at 0.001 s^{-1} is shown in Fig. 10 (a). It is seen that many dimples and tearing ridges are distributed on the uneven fracture surface. With increasing plastic deformation, instability initiates at comparatively weak places such as micro-voids and micro-cracks. During the growth of micro-voids, they coalesce with neighbors and form dimples with different sizes. During the propagation of micro-cracks, they interact and coalesce with each other, forming steps with tearing ridges. In addition, affected by the shear-tension stress state at the damage stage, as shown in Fig. 10 (b), part of the dimples is flattened out to be oval-shaped. Therefore, under quasi-static strain rates at room temperature, the specimen fails in a ductile failure mode with mixed features of shear and tension.

Under dynamic strain rates, the fracture pattern at 6000 s^{-1} is shown in Fig. 10 (c). Many dimples of various sizes are observed and the fracture surface is comparatively flatter than that at 0.001 s^{-1}. Compared to the quasi-static specimen, the dynamically loaded sample has larger and deeper dimples. This is because thermal softening due to adiabatic heating plays an important role in the failure process: during the growth and coalescence of dimples, large plastic deformation takes place. It is interesting to note that in Fig. 4 and 7, a significantly higher failure strain is observed at 0.001 s^{-1} ($\varepsilon_f > 80\%$) than at 6000 s^{-1} ($\varepsilon_f < 57\%$). At first sight, it may seem contradictory as in Fig. 10 larger plastic deformation is observed under dynamic loading by larger and deeper dimples. As a matter of fact, these observations are not in conflict because significantly improved ductility is achieved through the TRIP effect under quasi-static strain rates. During the deformation process, a fraction of the initial austenite phase transforms into the martensite phase. Due to the volume difference between the two phases [37] and the preferred orientations of the newly formed martensite phase [38], macroscopic transformation-induced plasticity develops. Under dynamic strain rates, affected by adiabatic heating and the reduced number of habit planes for martensite nucleation [39], the transformation process is strongly inhibited and the corresponding ductility decreases. In this work, according to martensite fraction measurement in post-mortem specimens by X-ray diffraction technique, 71±5% austenite phase transformed into martensite phase at 10^{-3} s^{-1}, which is three times the value for 6000 s^{-1} (23±3%).

Concerning the fracture morphology at the maximum strain rate of 39000 s^{-1}, the dimples are more severely stretched and many parabolic patterns are observed, Fig. 10 (d). The flow characteristics of dimple boundaries along the shear direction indicates an obvious temperature rise. Under such condition, the load capacity of 304 ASS evidently degrades. This explains why in Fig. 7 (f) the stress-strain curves show a negative strain hardening behavior. However, it should be noticed that no clear signs of well-developed adiabatic shear bands (ASBs) such as melting or irregular solidification grains are observed. The "disappearance" of ASBs is due to the shear-tension stress state at the fracture stage. ASBs are generated when the material is subjected to a shear-compression stress state with hydrostatic pressure over a short duration of less than 1 ms [40]. Hydrostatic pressure helps to delay the onset of damage micromechanism that develops within ASBs such as nucleation and growth of voids, and prolonged plasticity can be achieved [41]. Therefore, during shear tests under hydrostatic pressure, an obvious temperature increase is often observed either by high-speed infrared camera or through evidence such as recrystallization, melting and amorphization. Well-developed ASBs with the above characteristics are usually observed in hat-shaped specimens and SCS specimens where a shear-compression stress state with strong hydrostatic pressure exists [42–45]. In this work, the stress state in the specimen is shear-tension without hydrostatic pressure. Hence, the specimen fails via shear without well-developed ASBs. Similar phenomena were observed during dynamic torsion tests of tungsten alloy [40] and shear-tension tests of Ti–6Al–4V [46].

4. Thermo-viscoplastic behavior modeling

According to the shear behavior analysis in Section 3, a coupling effect between temperature and strain rate exists. Moreover, an enhanced strain rate sensitivity is observed at strain rates exceeding 13000 s^{-1}. Therefore, in this section, a modified Johnson-Cook (MJC) model incorporating these two aspects is proposed to describe the deformation behavior of 304 ASS. It should be noted that although martensitic transformation occurs in part of the shear tests, the characteristic S-shape flow stress curves and the second hardening phenomenon [12] are not observed in flow stress curves. Therefore, no special model formulation is used to describe martensitic transformation.

4.1. Modified Johnson-Cook (MJC) model proposition

Johnson-Cook (JC) model is a widely used phenomenological model describing deformation behavior of metallic materials over wide strain rate and temperature regimes. The original JC model is expressed as:

$$\sigma = (A + B\varepsilon^n)(1 + Cln\dot{\varepsilon}^*)(1 - T^{*m}) \tag{8}$$

where A, B, n, C and m are material parameters to be determined, $\dot{\varepsilon}^* = \dot{\varepsilon}/\dot{\varepsilon}_{ref}$ is the dimensionless strain rate and $T^* = (T - T_{ref})/(T_m - T_{ref})$ refers to the homologous temperature. T, T_m and T_{ref} are the absolute temperature, the melting temperature and the reference temperature, respectively. The three items of the JC model describe the strain hardening, strain rate sensitivity and thermal softening effect independently. In this section, taking the advantages of several variants of the original JC model [47–50] and the description of high rate stress upturn (HRSU) by Partom et al. [21–23], the MJC model is written as:

$$\sigma = [A + B(\dot{\varepsilon}, T)\varepsilon^{n_0}][1 + C(\dot{\varepsilon})]\left(\frac{T_m - T}{T_m - T_{ref}}\right)^m \tag{9}$$

where the particular form of $B(\dot{\varepsilon}, T)$ is defined as follow to describe the strain rate and temperature dependent strain hardening behavior. The overstress approach proposed by Partom et al. [21–23] is used to define in a better way the non-linear strain rate sensitivity $C(\dot{\varepsilon})$.

$$B(\dot{\varepsilon}, T) = B_0\left(1 - \frac{\ln\dot{\varepsilon}^*}{\ln\dot{\varepsilon}_{max}}\right)^{n_1}\left(\frac{T_m}{T}\right)^{n_2} \tag{10}$$

$$C(\dot{\varepsilon}) = 1 + \left(\frac{\dot{\varepsilon}}{\dot{\varepsilon}_0}\right)^{1/c_0} \tag{11}$$

where values of $\dot{\varepsilon}_{max}$ (the maximum strain rate experienced by the tested material) is 10^8 s^{-1}. A, B_0, n_1, n_2, n_0, c_0, $\dot{\varepsilon}_0$ and m are material constants to be determined.

For shear tests under dynamic strain rates ($\dot{\varepsilon} \geq 10\,s^{-1}$), the deformation process is regarded as 100% adiabatic and the corresponding temperature rise is estimated by Eq. (12):

$$\Delta T(\varepsilon) = \frac{\overline{\beta}}{\rho C_p}\int \sigma d\varepsilon \text{ with } T(\varepsilon) = T_0 + \Delta T(\varepsilon) \tag{12}$$

where ρ is the volumetric mass density of 304 ASS with a value of 7.8 g/

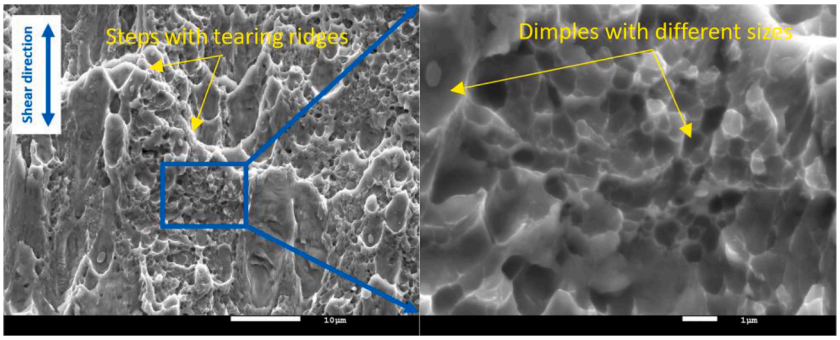

(a)

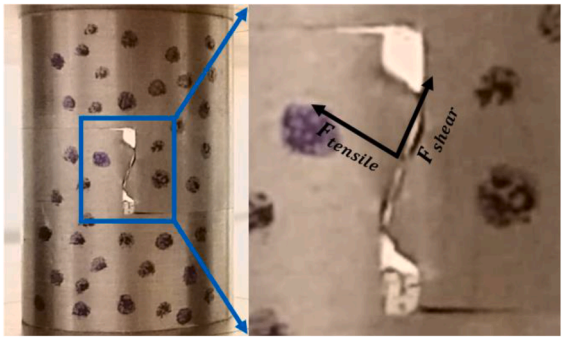

(b)

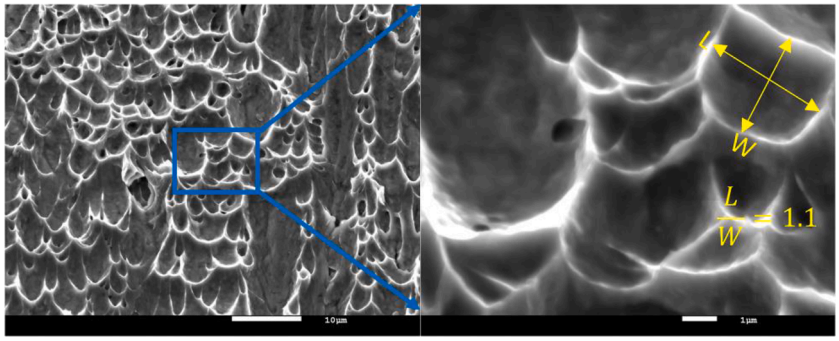

(c)

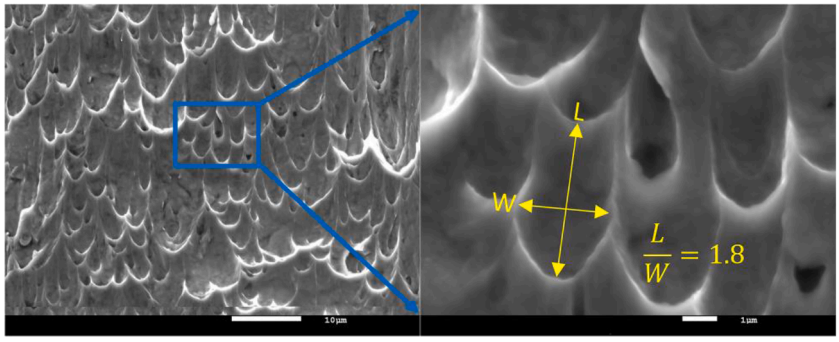

(d)

Fig. 10. Fracture surfaces of SSS specimens under different strain rates at room temperature: (a) 10^{-3} s^{-1} and (b) the macroscopic fracture pattern, (c) 6000 s^{-1} and (d) 39000 s^{-1}.

cm^3 and $\bar{\beta}$ is the average Taylor-Quinney coefficient characterizing the fraction of plastic work converted into heat. According to the work of Rusinek and Klepaczko [51], β is a non-linear function of plastic strain and the average value is chosen to be 0.9; C_p refers to the heat capacity of 304 ASS. Due to the low testing temperature encountered (77 K), C_p is given as a function of temperature instead of being a constant [52].

According to the shear stress-shear strain curves in Fig. 4 and 7, parameters of the MJC model are determined and shown in Table 3.

4.2. Description capacity of the MJC model

A comparison of stress-strain curves between experiments and model predictions is shown in Fig. 11. To assess the predictive capability of the constitutive model quantitatively, the prediction error Δ is calculated by

$$\Delta = \frac{1}{N}\sum_{i=1}^{N}\left|\frac{\sigma_i^{exp} - \sigma_i^{pre}}{\sigma_i^{exp}}\right| \times 100\% \tag{13}$$

where σ_i^{exp} and σ_i^{pre} are the flow stresses obtained from experiments and predicted by the MJC model, respectively. The prediction error for the MJC model is shown in Fig. 11 (i).

For the two quasi-static strain rates, the model predicts the flow stress curves at 77 and 293 K accurately but gives overestimated flow stresses at 473 K. The average prediction errors for 0.001 and 0.1 s^{-1} are respectively 3.76% and 4.30%. For dynamic strain rates between 3000 and 26000 s^{-1}, the model gives fairly good predictions in terms of both flow stress level and strain hardening rate, and the prediction errors are always below 4.5%. At the maximum strain rate of 39000 s^{-1}, the model gives positive strain hardening rates while the values are negative in experiments, and this leads to a prediction error of 5.48%.

To study the predictive capability of the MJC model more in details, the experimental strain rate and temperature sensitivities are compared to the model predictions, Fig. 12. It is seen from Fig. 12 (a) that the MJC model gives nonlinear strain rate sensitivity predictions. In quasi-static tests, the predicted flow stress by the MJC model is consistent with experiments with an average error of 5.44%. In dynamic tests, the model predicts an abrupt flow stress increase with logarithmic strain rate and agrees with experiments well. The discontinuity in flow stress curves is caused by the adiabatic heating effect in dynamic strain rates ($\dot{\varepsilon} \geq 10\,s^{-1}$) while this phenomenon is not taken into account for quasi-static tests. In Fig. 14 (b), the decreasing flow stress level with increasing temperature is predicted correctly by the model. In summary, the MJC model can be used to predict simple shear behavior of 304 ASS accurately.

4.3. Finite element analysis of dynamic shear tests

To validate the previously established MJC model, numerical simulations of simple shear tests have been conducted using ABAQUS Explicit. The 3D finite element (FE) model consists of an incident bar, a transmitted bar and an SSS specimen sandwiched between them, Fig. 13. The projectile is not included and the experimentally obtained force-time curves are applied on the end face of the incident bar. Frictional contact with a coefficient of 0.1 is assumed at the specimen/bar interfaces. For incident and transmitted bars, the 8-node linear brick with reduced integration element C3D8R is selected. For SSS specimen, the coupled displacement-temperature 8 nodes element with full integration C3D8T is used. To improve computational efficiency, different mesh sizes are used for different parts of the FE model. 10 mm and 1 mm elements are used along the axial and the radial directions of the SHPB bars, respectively. Global element size of the SSS specimen is 0.5 mm and is further refined to be 0.02 mm in the shear zone. The total numbers of element for SHPB bars and SSS specimen are 101120 and 157663, respectively.

Material properties of different parts of the FE model are shown in Table 4. The incident and transmitted bars are regarded as elastic instances with Young's modulus of 210 GPa, while the previously determined MJC model is used to describe the deformation behavior of the SSS specimen.

A comparison of force wave signals between experiments and numerical simulations at strain rate of 13000 s^{-1} is shown in Fig. 14. It is observed that from 340 to 411 μs, corresponding to the plastic deformation period of the shear zone, the experimental force wave signals agree with the numerical predictions, with an average error of 5.4%. Both the flow stress and strain hardening rate are correctly captured by the model. After that, failure occurs in experiments while this process is not considered in the numerical simulation. Therefore, the experimental signal starts to decrease and deviates from the numerical result. In general, the MJC model provides an accurate prediction of the force wave signals.

Based on the numerical results shown in Fig. 14, a comparison between the average stress-strain relation of all elements in the shear zone (representing the input model to Abaqus) and the experimentally measured stress-strain curve (representing the real shear behavior of 304 ASS) is shown in Fig. 15. It is observed that the numerical flow stress curves are consistent with the experiments with an average error of 2.8%. In fact, the two curves coincide if the signal oscillation is ignored. Both the yield stresses and the strain hardening rates are correctly predicted. This observation is consistent with the flow stress curves shown in Fig. 11.

The utility of a constitutive model lies in not only its capability of fitting experimentally obtained flow stress curves but also its ability to predict deformation behavior beyond the testing conditions. To further evaluate the determined MJC model, another shear test at strain rate of 11000 s^{-1}, which is not used for the identification of the MJC model parameters, has been performed. Different from the previously defined testing rules where the SSS specimen with $L = 1$ mm should be used for testing at strain rates below 15000 s^{-1}, the specimen with $L = 0.5$ mm was used in this test. A comparison of flow stress curves between experiment and numerical simulation is shown in Fig. 16. It is seen that the MJC model can reproduce the stress-strain curves correctly with an average error of 2.5%. The trends of yield stress and strain hardening rate are correctly captured. Therefore, although SSS specimens with different shear zone widths are assigned to various strain rate regimes, the error due to the different specimen dimensions can be effectively eliminated by the correction coefficient method. The experimentally measured flow stress curves represent the correct shear behavior of 304 ASS.

According to the numerical results for shear tests at 11000 s^{-1}, the stress state in the specimen shear zone is analyzed. First, the variation of the average stress components of the whole shear zone is shown in Fig. 17 (a). For comparison, the numerical data of a classical double shear specimen (DSS) proposed by Klepaczko [18] is shown in Fig. 17 (b). It is seen from Fig. 17 (a) that during the plastic deformation process, the shear zone is dominated by shear stress component σ_{13}. The absolute value increases monotically from 635 MPa at $\gamma = 0$ to 1015 MPa at the damage initiation point. For the other stress components, they are either significantly smaller (σ_{11} and σ_{22}) or remain at zero (σ_{12}, σ_{23} and σ_{33}). In Fig. 17 (b), the evolution of shear stress components (σ_{12}, σ_{13} and σ_{23}) in DSS specimen is similar to that in SSS specimen but the normal stress components (σ_{11}, σ_{22} and σ_{33}) are comparatively higher. For example, in SSS specimen, the absolute value of σ_{11} decreases from 181 to 0 MPa first and then remains at zero at larger deformation; while for the DSS specimen, σ_{11} increases monotonically from 0 MPa at $\gamma = 0$ to 430 MPa at the damage initiation point. This is

Table 3
Determined parameters of the MJC model.

A (MPa)	B_0 (MPa)	c_0	m	n_0	n_1	n_2	$\dot{\varepsilon}_0$
1102	302	1.933	1.644	1.089	-0.653	0.654	120000

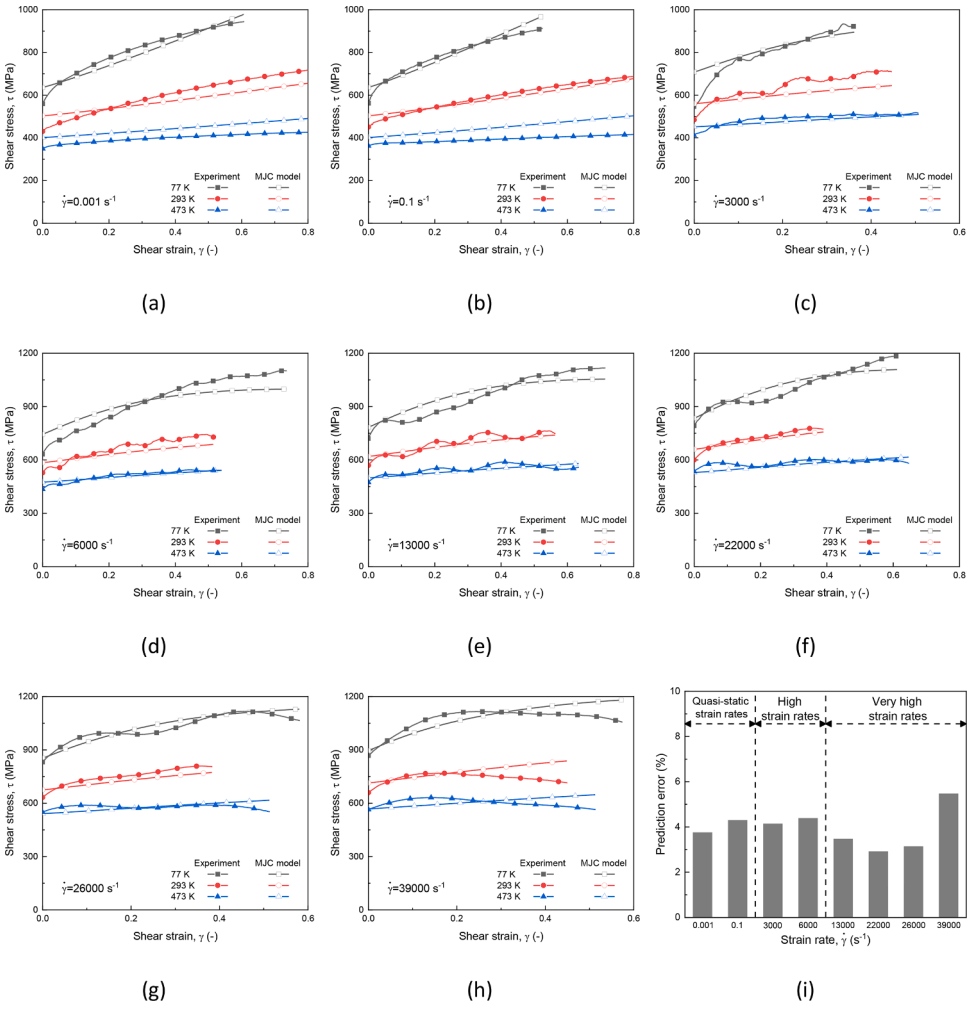

Fig. 11. Comparison of flow stress curves between experiments and MJC model predictions for indicated strain rates and temperatures.

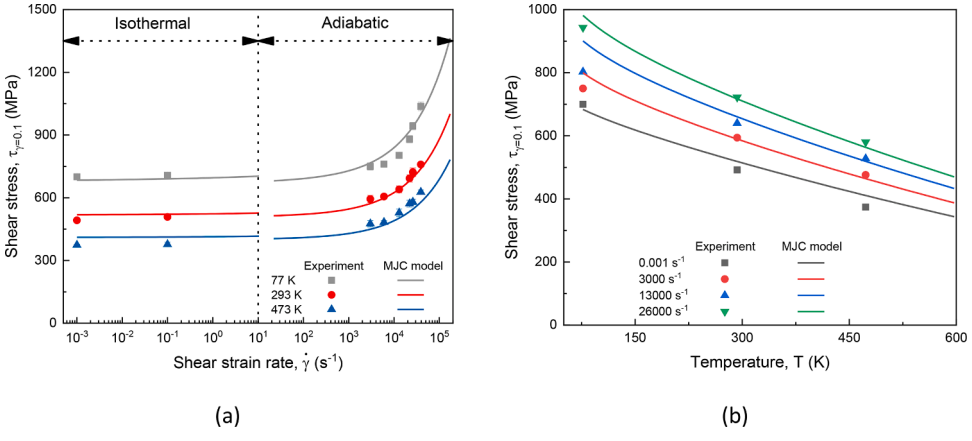

Fig. 12. Comparison of (a) strain rate sensitivity and (b) temperature sensitivity between experiments and model predictions.

because σ_{11} is the stress component characterizing the stress state along the shear zone width direction (the indicated X axis in Fig. 18). In DSS specimen, as shown in Fig. 18, clamping devices are needed to prevent specimen rotation and achieve a uniform distribution of stress components [18,53]. A disadvantage of this design is that the lateral displacement of the shear zone is inhibited and a tensile stress component appears. On the contrary, for SSS specimen, it moves freely in both longitudinal and lateral directions. Therefore, the tensile stress component σ_{11} is suppressed. In summary, the deformation process in both SSS and DSS specimens is dominated by shear stress component σ_{13} while the others are comparatively smaller. However, compared to the latter, a stress state closer to pure shear is achieved in the SSS specimen.

At the damage initiation point, the distributions of Von Mises stress and equivalent plastic strain in the SSS specimen are shown in Fig. 19 and 20, respectively. It is observed from Fig. 19 that Von Mises stress is uniformly distributed in the shear zone and the value varies between

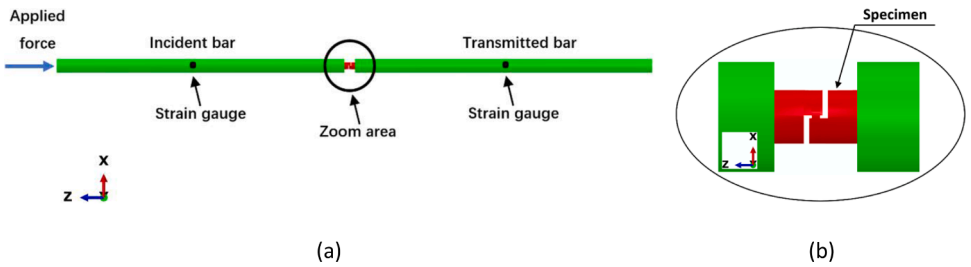

Fig. 13. FE model for numerical simulations: (a) the assembly including the incident bar, the transmitted bar and the SSS specimen and (b) magnification of the SSS specimen.

Table 4
Material properties of different parts of the FE model.

Part	Material	ρ (kg/m^3)	E (GPa)	Poisson's ratio, μ	Thermal conductivity, λ (W/m•°C)
SSS specimen	304 ASS	7800	210	0.3	16.2
SHPB bars	Maraging steel	8200	210	0.3	(-)

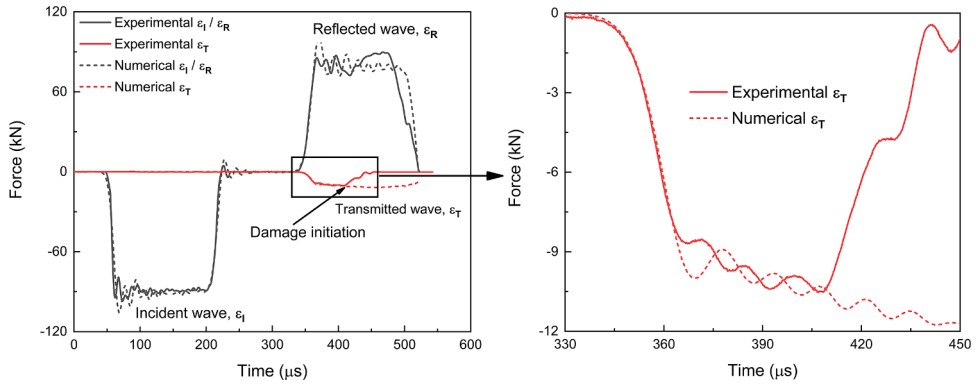

Fig. 14. Comparison of force wave signals between experiments and numerical simulations by the MJC model at strain rate of 13000 s^{-1}.

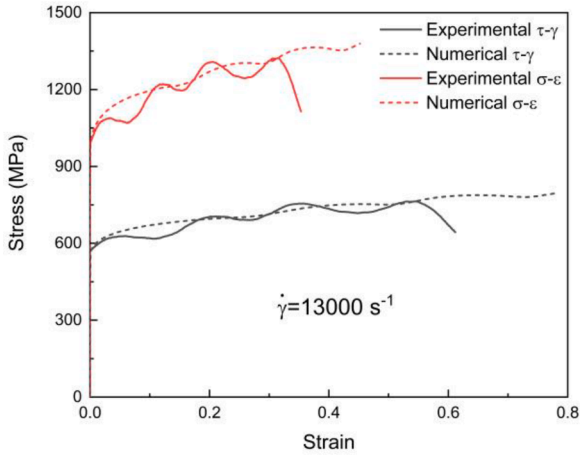

Fig. 15. Comparison of flow stress curves between experiments and numerical simulations by the MJC model at strain rate of 13000 s^{-1}.

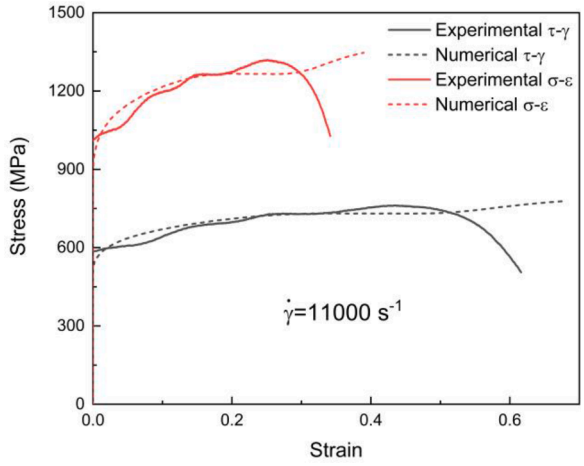

Fig. 16. Comparison of flow stress curves between experiments and numerical simulations by the MJC model at strain rate of 11000 s^{-1}.

1300 and 1750 MPa. At the four corners of the shear zone, the highest values are observed due to stress concentration. Affected by the single shear zone design, from the shear zone to the other parts of the specimen, the distribution of Von Mises stress is axisymmetric. In Fig. 20 (a), equivalent plastic strain is uniformly distributed in the shear zone while the surrounding structure remains elastic. A strain concentration at the four corners of the shear zone is observed, with the top left and bottom right regions being the highest (0.71) while the other two regions being comparatively smaller (0.42). According to the distribution of equivalent plastic strain, the SSS specimen tends to fail along the diagonal direction (top left-bottom right) of the shear zone. Besides, failure behavior of metallic materials is known to be strongly affected by stress state and early fracture is commonly observed at large stress triaxiality conditions [54]. Considering the distribution of stress triaxiality in the shear zone ($\eta_{top\ left} = -0.47$; $\eta_{top\ right} = 0.67$;) shown in Fig. 20 (a), the SSS specimen tends to fail along the other diagonal direction (top right-bottom left). Therefore, taking the distribution of both equivalent

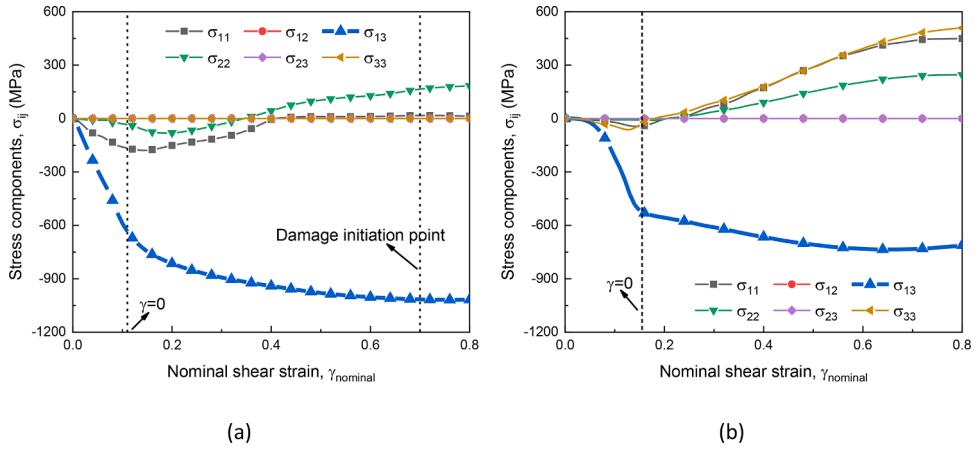

Fig. 17. Variation of the average stress components in shear zones of the (a) SSS specimen and (b) DSS specimen.

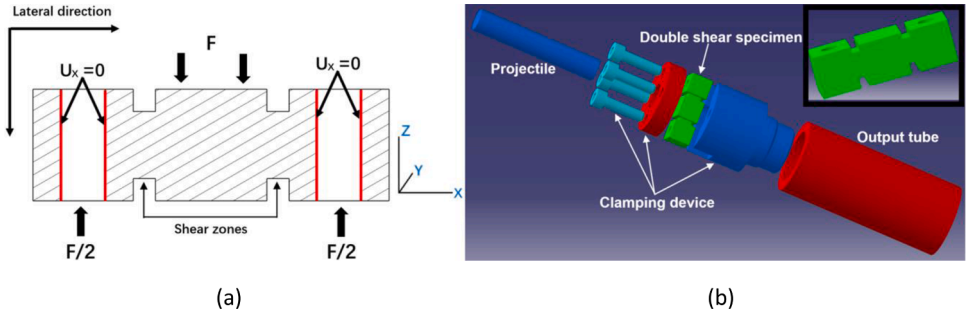

Fig. 18. Schematic view of the classical DSS specimen: (a) boundary conditions and (b) practical arrangement.

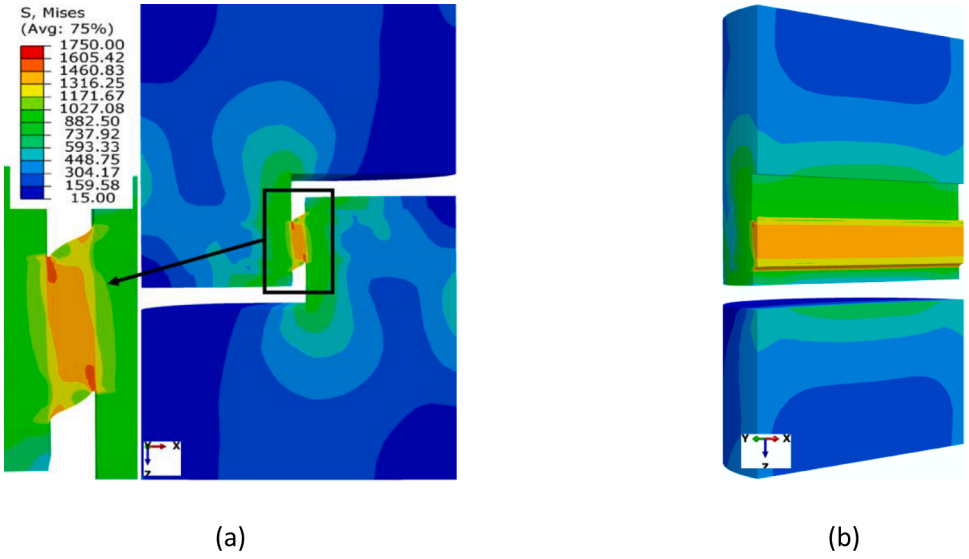

Fig. 19. Distribution of Von Mises stress at the damage initiation point: (a) on the central y-z plane and (b) on the central x-z plane.

plastic strain and stress triaxiality into consideration, either diagonal or non-diagonal failure may occur. This finding is consistent with the experimental results where both failure along the diagonal direction of the shear zone is observed in Fig. 10 (b) and fracture propagation along the non-diagonal direction is recorded by the high-speed camera in Fig. 6.

From the numerical simulations, the stress state in the shear zone is analyzed. Stress state can be described by two parameters: stress triaxiality η and Lode angle parameter $\overline{\theta}$. η is defined as the ratio of the hydrostatic stress σ_m to the Von Mises stress $\overline{\sigma}$, while $\overline{\theta}$ is a function of the third invariant of the stress deviator and is used to represent the different stress states with the same η value in three dimensions.

$$\eta = \frac{\sigma_m}{\overline{\sigma}} = \frac{\sqrt{2}(\sigma_1 + \sigma_2 + \sigma_3)}{3\sqrt{(\sigma_1 - \sigma_2)^2 + (\sigma_2 - \sigma_3)^2 + (\sigma_3 - \sigma_1)^2}} \tag{14}$$

$$\overline{\theta} = \frac{(2\sigma_2 - \sigma_1 - \sigma_3)}{\sigma_1 - \sigma_3} \tag{15}$$

where σ_1, σ_2 and σ_3 are the three principal stresses following the order

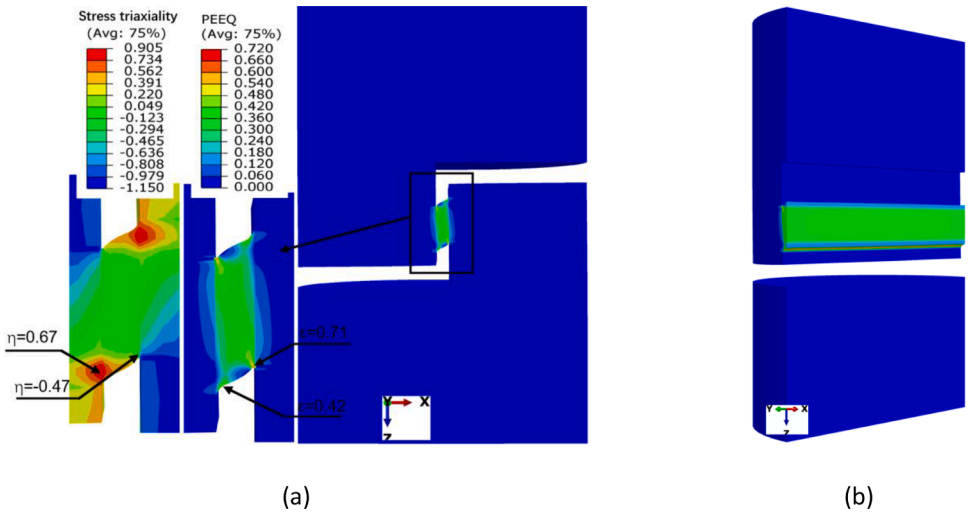

Fig. 20. Distribution of equivalent plastic strain at the damage initiation point: (a) on the central y-z plane and (b) on the central x-z plane.

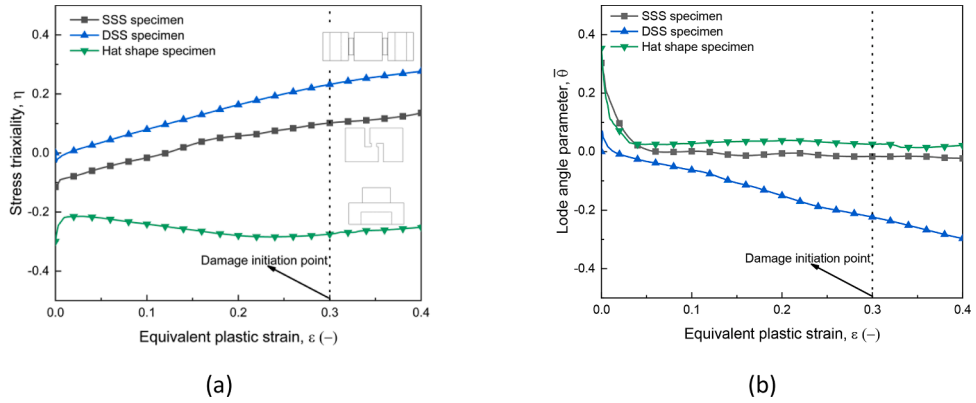

Fig. 21. Variation of average stress state parameters of the whole shear zone with plastic strain: (a) stress triaxiality η and (b) Lode angle parameter $\overline{\theta}$.

$\sigma_1 \geq \sigma_2 \geq \sigma_3$. The average stress state (η, $\overline{\theta}$) in the shear zone is shown in Fig. 21. Besides, the classical double shear specimen and hat shape specimen, which may be used for shear tests under very high strain rates above 10^4 s^{-1}, are also depicted for comparison. For the SSS specimen, stress triaxiality η increases slightly from -0.10 at ε_{eq}=0 to 0.10 at the damage initiation point, while Lode angle parameter $\overline{\theta}$ shows an opposite tendency. During the plastic deformation process, the average values of η and $\overline{\theta}$ are respectively 0.015 and 0.014. Therefore, a simple shear stress state is obtained in the SSS specimen. For the DSS specimen, variation of η and $\overline{\theta}$ is similar but the corresponding absolute values are comparatively higher. The average values of η and $\overline{\theta}$ are respectively 0.115 and -0.112, indicating a shear-tension stress state. Concerning hat shape specimen, stress triaxiality η remains almost constant at -0.258 and a shear-compression stress state with hydrostatic pressure exists. On the whole, compared to DSS and hat shape specimens, the novel SSS specimen can be used for more accurate characterization of simple shear behavior.

5. Conclusion

A novel single shear specimen (SSS) together with a correction coefficient method has been used to study the deformation behavior of a 304 stainless steel under shear loading. Shear stress-shear strain curves over a wide range of shear strain rates (0.001 to 39000 s^{-1}) at three initial temperatures (77, 293 and 473 K) are obtained. The effects of strain rate and temperature on the flow stress curves are investigated. The fracture morphology of the specimens is analyzed. Based on the experimentally obtained shear stress-shear strain curves, parameters of a modified Johnson-Cook (MJC) model are determined and the model prediction capability is validated. Using finite element analysis, the distribution of stress and strain components as well as stress state in the shear zone are analyzed. The main findings are summarized as follows.

1 The flow stress is a non-linear function of strain rate: it remains constant in quasi-static strain rates regime and then increases slightly at strain rates between 0.1 to 6000 s^{-1}; at higher strain rates, a rapid increase is observed. Sensitivity to strain rate is also observed for the strain hardening rate: with increasing strain rate, the value decreases monotonically. In particular, at the maximum strain rate of 39000 s^{-1}, a negative strain hardening behavior was observed, indicating a strong adiabatic temperature rise.
2 No well-developed adiabatic shear bands were observed in dynamic shear tests, even at the maximum strain rate of 39000 s^{-1}. This may be due to the shear-tension stress state without the presence of hydrostatic pressure in the fracture process.
3 The MJC model shows a capability to predict the flow stress curves. Although no special model formulation is used to describe martensitic transformation, both the flow stress and the strain hardening rate are correctly reproduced. Besides, the predicted strain wave signals are consistent with the experiments.
4 According to numerical simulations, the deformation process of SSS specimen is dominated by shear stress and shear strain components, while the other components are obviously smaller. A simple shear stress state is obtained in the shear zone. The average stress

triaxiality η and Lode angle parameter $\overline{\theta}$ are respectively 0.015 and 0.014, which are closer to zero than those for the classical DSS ($\eta = 0.115$, $\overline{\theta} = -0.112$) and hat shape ($\eta = -0.258$, $\overline{\theta} = 0.038$) specimens.

Author Statement

Bin Jia: Mechanical tests, Numerical simulations, Data analysis, Writing – original manuscript; Alexis Rusinek: Supervision, Writing – review and editing; Raphaël Pesci: Supervision, Writing – review and editing; Richard Bernier: Mechanical tests, Data analysis; Slim Bahi: Numerical simulations, Data analysis; Amine Bendarma: Numerical simulations, Data analysis; Paul Wood: Numerical simulations, Data analysis

Appendix A. Supplementary data

Supplementary data associated with this manuscript can be found in the uploaded video named dynamic shear testing by a high speed camera.

Declaration of Competing Interest

The authors declare that they have no known competing financial interests or personal relationships that could have appeared to influence the work reported in this paper.

Acknowledgements

This work of the first author was financially supported by the China Scholarship Council under Grant 201606220056.

Supplementary materials

Supplementary material associated with this article can be found, in the online version, at doi:10.1016/j.ijimpeng.2021.103896.

References

[1] Fischer FD, Sun Q-P, Tanaka K. Transformation-Induced Plasticity (TRIP). Appl Mech Rev 1996;49:317–64. https://doi.org/10.1115/1.3101930.
[2] Song S, Gui-bao D, Zu-Ping D. Martensitic transformation under impact with high strain rate. Int J Impact Eng 2001;25:755–65. https://doi.org/10.1016/S0734-743X(01)00016-1.
[3] Byun TS, Hashimoto N, Farrell K. Temperature dependence of strain hardening and plastic instability behaviors in austenitic stainless steels. Acta Mater 2004;52:3889–99. https://doi.org/10.1016/j.actamat.2004.05.003.
[4] Hamada AS, Karjalainen LP, Misra RDK, Talonen J. Contribution of deformation mechanisms to strength and ductility in two Cr–Mn grade austenitic stainless steels. Mater Sci Eng A 2013;559:336–44. https://doi.org/10.1016/j.msea.2012.08.108.
[5] Zheng C, Yu W. Effect of low-temperature on mechanical behavior for an AISI 304 austenitic stainless steel. Mater Sci Eng A 2018;710:359–65. https://doi.org/10.1016/j.msea.2017.11.003.
[6] Yoo S-W, Lee C-S, Park W-S, Kim M-H, Lee J-M. Temperature and strain rate dependent constitutive model of TRIP steels for low-temperature applications. Comput Mater Sci 2011;50:2014–27. https://doi.org/10.1016/j.commatsci.2011.02.002.
[7] Qin Z, Xia Y. Role of strain-induced martensitic phase transformation in mechanical response of 304L steel at different strain-rates and temperatures. J Mater Process Technol 2020;280:116613. https://doi.org/10.1016/j.jmatprotec.2020.116613.
[8] Lichtenfeld JA, Van Tyne CJ, Mataya MC. Effect of strain rate on stress-strain behavior of alloy 309 and 304L austenitic stainless steel. Metall Mater Trans A 2006;37:147–61. https://doi.org/10.1007/s11661-006-0160-5.
[9] Rahmaan T, Bardelcik A, Imbert J, Butcher C, Worswick MJ. Effect of strain rate on flow stress and anisotropy of DP600, TRIP780, and AA5182-O sheet metal alloys. Int J Impact Eng 2016;88:72–90. https://doi.org/10.1016/j.ijimpeng.2015.09.006.
[10] Hecker SS, Stout MG, Staudhammer KP, Smith JL. Effects of Strain State and Strain Rate on Deformation-Induced Transformation in 304 Stainless Steel: Part I. Magnetic Measurements and Mechanical Behavior. Metall Trans A 1982;13:619–26. https://doi.org/10.1007/BF02644427.
[11] Murr LE, Staudhammer KP, Hecker SS. Effects of Strain State and Strain Rate on Deformation-Induced Transformation in 304 Stainless Steel: Part II. Microstructural Study. Metall Trans A 1982;13:627–35. https://doi.org/10.1007/BF02644428.
[12] Jia B, Rusinek A, Pesci R, Bahi S, Bernier R. Thermo-viscoplastic behavior of 304 austenitic stainless steel at various strain rates and temperatures: Testing, modeling and validation. Int J Mech Sci 2020;170:105356. https://doi.org/10.1016/j.ijmecsci.2019.105356.
[13] Xu Z, Liu Y, Hu H, He X, Huang F. Thermo-viscoplastic behavior and constitutive modeling of pure copper under high-strain-rate shear condition. Mech Mater 2019;129:306–19. https://doi.org/10.1016/j.mechmat.2018.12.007.
[14] Xu Z, Liu Y, Hu H, He X, Huang F. Determination of shear behavior and constitutive modeling of the 603 steel over wide temperature and strain rate ranges. J Mech Phys Solids 2019;129:184–204. https://doi.org/10.1016/j.jmps.2019.05.005.
[15] Follansbee PS, Kocks UF. A constitutive description of the deformation of copper based on the use of the mechanical threshold stress as an internal state variable. Acta Metall 1988;36:81–93. https://doi.org/10.1016/0001-6160(88)90030-2.
[16] Tong W, Clifton RJ, Huang S. Pressure-shear impact investigation of strain rate history effects in oxygen-free high-conductivity copper. J Mech Phys Solids 1992;40:1251–94. https://doi.org/10.1016/0022-5096(92)90015-T.
[17] Huang S, Clifton RJ. Macro and Micro-Mechanics of High Velocity Deformation and Fracture. Tokyo: IUTAM; 1985. p. 63–74.
[18] Klepaczko JR. An experimental technique for shear testing at high and very high strain rates. The case of a mild steel. Int J Impact Eng 1994;15:25–39. https://doi.org/10.1016/S0734-743X(05)80005-3.
[19] Rusinek A, Rodríguez-Martínez JA. Thermo-viscoplastic constitutive relation for aluminium alloys, modeling of negative strain rate sensitivity and viscous drag effects. Mater Design 2009;30:4377–90. https://doi.org/10.1016/j.matdes.2009.04.011.
[20] Nemat-Nasser S, Guo W-G, Kihl DP. Thermomechanical response of AL-6XN stainless steel over a wide range of strain rates and temperatures. J Mech Phys Solids 2001;49:1823–46. https://doi.org/10.1016/S0022-5096(00)00069-7.
[21] Partom Yehuda. Modeling stress upturn at high strain rates for ductile materials. EPJ Web Conf 2018;183:01002. https://doi.org/10.1051/epjconf/201818301002.
[22] Partom Y. The role of strain rate in the dynamic response of materials. IJCMP 2020;4:9–17. https://doi.org/10.22161/ijcmp.4.1.3.
[23] Partom Y. Modeling high rate stress upturn for brittle materials. AIP Conf Proc 2020;2272:100019. https://doi.org/10.1063/12.0000885.
[24] Gao CY, Zhang LC. Constitutive modelling of plasticity of fcc metals under extremely high strain rates. Int J Plast 2012;32–33:121–33. https://doi.org/10.1016/j.ijplas.2011.12.001.
[25] Arab A, Guo Y, Zhou Q, Chen P. A New S-Shape Specimen for Studying the Dynamic Shear Behavior of Metals. Metals 2019;9. https://doi.org/10.3390/met9080838.
[26] Jia B, Rusinek A, Pesci R, Bernier R, Bahi S, Wood P. A novel technique for dynamic shear testing of bulk metals with application to 304 austenitic stainless steel. Int J Solids Struct 2020. https://doi.org/10.1016/j.ijsolstr.2020.08.019.
[27] Zhong WZ, Rusinek A, Jankowiak T, Abed F, Bernier R, Sutter G. Influence of interfacial friction and specimen configuration in Split Hopkinson Pressure Bar system. Tribol Int 2015;90:1–14. https://doi.org/10.1016/j.triboint.2015.04.002.
[28] Rusinek A, Klepaczko JR. Shear testing of a sheet steel at wide range of strain rates and a constitutive relation with strain-rate and temperature dependence of the flow stress. Int J Plast 2001;17:87–115. https://doi.org/10.1016/S0749-6419(00)00020-6.
[29] Dorogoy A, Rittel D, Godinger A. Modification of the Shear-Compression Specimen for Large Strain Testing. Exp Mech 2015;55:1627–39. https://doi.org/10.1007/s11340-015-0057-6.
[30] Shi FF, Merle R, Hou B, Liu JG, Li YL, Zhao H. A critical analysis of plane shear tests under quasi-static and impact loading. Int J Impact Eng 2014;74:107–19. https://doi.org/10.1016/j.ijimpeng.2014.06.012.
[31] Campbell JD, Ferguson WG. The temperature and strain-rate dependence of the shear strength of mild steel, The Philosophical Magazine: A. J Theo Exp Applied Physics 1970;21:63–82. https://doi.org/10.1080/14786437008238397.
[32] Guo Y, Li Y. A Novel Approach to Testing the Dynamic Shear Response of Ti-6Al-4V. Acta Mech Solida Sin 2012;25:299–311. https://doi.org/10.1016/S0894-9166(12)60027-5.
[33] Fras T. Modelling of plastic yield surface of materials accounting for initial anisotropy and strength differential effect on the basis of experiments and numerical simulation. PhD Thesis. Université de Lorraine; 2013.
[34] Klepaczko JR, Rusinek A, Rodríguez-Martínez JA, Pęcherski RB, Arias A. Modelling of thermo-viscoplastic behaviour of DH-36 and Weldox 460-E structural steels at wide ranges of strain rates and temperatures, comparison of constitutive relations for impact problems. Mech Mater 2009;41:599–621. https://doi.org/10.1016/j.mechmat.2008.11.004.
[35] Kocks UF, Argon AS, Ashby MF. Thermodynamics and Kinetics of Slip. Argonne National Laboratory; 1973. https://books.google.fr/books?id=4LI-pwAACAAJ.
[36] Nemat-Nasser S, Guo W-G. Thermomechanical response of DH-36 structural steel over a wide range of strain rates and temperatures. Mech Mater 2003;35:1023–47. https://doi.org/10.1016/S0167-6636(02)00323-X.
[37] Greenwood GW, Johnson RH. The deformation of metals under small stresses during phase transformations. Procee Royal Soc London Series A Math Phys Sci 1965;283:403–22.
[38] Magee CL, Paxton HW. Transformation kinetics, microplasticity and aging of martensite in FE-31 NI. CARNEGIE INST OF TECH PITTSBURGH PA; 1966.
[39] Vázquez-Fernández NI, Nyyssönen T, Isakov M, Hokka M, Kuokkala V-T. Uncoupling the effects of strain rate and adiabatic heating on strain induced martensitic phase transformations in a metastable austenitic steel. Acta Mater 2019;176:134–44. https://doi.org/10.1016/j.actamat.2019.06.053.

[40] Dodd B, Bai Y. Adiabatic Shear Localization: Frontiers and Advances. Elsevier; 2012.
[41] Hanina E, Rittel D, Rosenberg Z. Pressure sensitivity of adiabatic shear banding in metals. Appl Phys Lett 2007;90:021915. https://doi.org/10.1063/1.2430923.
[42] Bronkhorst CA, Cerreta EK, Xue Q, Maudlin PJ, Mason TA, Gray GT. An experimental and numerical study of the localization behavior of tantalum and stainless steel. Int J Plast 2006;22:1304–35. https://doi.org/10.1016/j.ijplas.2005.10.002.
[43] Minnaar K, Zhou M. An analysis of the dynamic shear failure resistance of structural metals. J Mech Phys Solids 1998;46:2155–70. https://doi.org/10.1016/S0022-5096(98)00020-9.
[44] Chichili DR, Ramesh KT, Hemker KJ. Adiabatic shear localization in α-titanium: experiments, modeling and microstructural evolution. J Mech Phys Solids 2004;52:1889–909. https://doi.org/10.1016/j.jmps.2004.02.013.
[45] Rittel D, Landau P, Venkert A. Dynamic Recrystallization as a Potential Cause for Adiabatic Shear Failure. Phys Rev Lett 2008;101:165501. https://doi.org/10.1103/PhysRevLett.101.165501.
[46] Zhu S, Guo Y, Chen H, Li Y, Fang D. Formation of adiabatic shear band within Ti–6Al–4V: Effects of stress state. Mech Mater 2019;137:103102. https://doi.org/10.1016/j.mechmat.2019.103102.
[47] Farrokh B, Khan AS. Grain size, strain rate, and temperature dependence of flow stress in ultra-fine grained and nanocrystalline Cu and Al: Synthesis, experiment, and constitutive modeling. Int J Plast 2009;25:715–32. https://doi.org/10.1016/j.ijplas.2008.08.001.
[48] Khan AS, Liang R. Behaviors of three BCC metal over a wide range of strain rates and temperatures: experiments and modeling. Int J Plast 1999;15:1089–109. https://doi.org/10.1016/S0749-6419(99)00030-3.
[49] Khan AS, Farrokh B. Thermo-mechanical response of nylon 101 under uniaxial and multi-axial loadings: Part I, Experimental results over wide ranges of temperatures and strain rates. Int J Plast 2006;22:1506–29. https://doi.org/10.1016/j.ijplas.2005.10.001.
[50] Couque H. The use of the direct impact Hopkinson pressure bar technique to describe thermally activated and viscous regimes of metallic materials. Philos Trans R Soc, A 2014;372:20130218. https://doi.org/10.1098/rsta.2013.0218.
[51] Rusinek A, Klepaczko JR. Experiments on heat generated during plastic deformation and stored energy for TRIP steels. Mater Design 2009;30:35–48. https://doi.org/10.1016/j.matdes.2008.04.048.
[52] Jia B, Rusinek A, Bahi S, Bernier R, Pesci R, Bendarma A. Perforation Behavior of 304 Stainless Steel Plates at Various Temperatures. J Dynam Behav Mater 2019:1–16. https://doi.org/10.1007/s40870-019-00208-9.
[53] Xu Z, Ding X, Zhang W, Huang F. A novel method in dynamic shear testing of bulk materials using the traditional SHPB technique. Int J Impact Eng 2017;101:90–104. https://doi.org/10.1016/j.ijimpeng.2016.11.012.
[54] Bao Y, Wierzbicki T. On fracture locus in the equivalent strain and stress triaxiality space. Int J Mech Sci 2004;46:81–98. https://doi.org/10.1016/j.ijmecsci.2004.02.006.